

# Magnetic graphene oxide/carboxymethyl-imidazolium-grafted chitosan Schiff base nanocomposite: a new PdNPs support for efficient catalytic reduction of hazardous nitroarenes

Rana Yahya (✉ [royahiya@yahoo.com](mailto:royahiya@yahoo.com))

University of Jeddah

---

## Research Article

**Keywords:** Carboxymethyl-imidazolium chitosan Schiff base, Magnetic nanocomposites, Nitroarenes reduction

**Posted Date:** March 15th, 2022

**DOI:** <https://doi.org/10.21203/rs.3.rs-1447305/v1>

**License:**  This work is licensed under a Creative Commons Attribution 4.0 International License.

[Read Full License](#)

---

# Abstract

The relevance of aryl amines as raw materials for a variety of applications has prompted substantial research into developing highly efficient protocols for hazardous nitroarenes reduction. To that end, a new sustainable and heterogeneous palladium nanocatalyst was fabricated by immobilization of PdNPs on the new magnetic support composed of carboxymethyl-imidazolium ionic liquid-grafted chitosan Schiff base and magnetic graphene oxide (CMICSB-MGO) nanocomposites. The spectral, thermal, and microscopic analyses results revealed the successful formation of the magnetic support and nanocatalyst. The activity of the new nanocatalyst (CMICSB-MGO-Pd) in the catalytic reduction of hazardous nitroarenes to convert them into valuable aminoarenes was studied. The findings demonstrated that the new nanocatalyst has excellent catalytic activity, superior recoverability, as well as outstanding reusability under very mild reaction conditions. Moreover, this nanocatalyst can be recycled up to 8 catalytic runs, without significant loss in its efficacy or Pd leaching. Thus, the new magnetic support and nanocatalyst are more eco-friendly and sustainable choices for large-scale use and could pave the way for developing other metal-based catalysts for versatile applications in the future.

## 1. Introduction

In the last few years, "green chemistry" strategies have received great attention from a huge number of researchers worldwide. This interest has been extended to involve all aspects of environmental and industrial chemistry [1,2,3]. Catalysts act as pivotal and very important mediators in most industrial chemical processes. Although homogeneous catalysts have excellent performance, high selectivity, and easy optimization, their difficult recovery, reusability, and probabilistic toxicity limit their use in industrial applications [4]. Therefore, heterogeneous (supported) catalysts have strongly invaded the industrial field to tackle the problems associated with homogeneous catalysts [4,5]. Nevertheless, heterogeneous catalyst suffers some limitations due to the difficult accessibility of catalytic active sites and low diffusion characteristics, causing lower efficacy as compared to homogeneous catalyst [4]. Therefore, exploring catalytic systems possessing not only high activity and selectivity (as in homogeneous catalysis) but also being easily recoverable and reusable (as in heterogeneous catalysis) is necessary.

To that end, many industrial and academic research groups have developed a variety of supported ionic liquid catalysts (SILCs) as green catalytic systems for various applications [6,7]. Notably, the SILC is composed of an ionic liquid (IL) layer embedded with the homogeneous catalyst and immobilized on the surface of solid support. The catalyst-loaded ionic liquid layer behaves as a homogeneous phase with enhanced diffusion properties and higher activity, while the immobilization on a porous support allows facile isolation of the product, potential reusability of the catalyst, and continuous catalytic process [8]. The SILCs were initially developed using inorganic supports like SBA-15 [9] and heteropolyacids [10]. Recently, green supports such as biopolymers (chitin, chitosan, cellulose, alginates, and cyclodextrin) [11], lignin [11], and graphene oxide [12] have been used to reduce the negative impacts of the inorganic supports. To boost catalytic capabilities, the support should offer a large surface area to facilitate

diffusion. Additionally, the elaboration of novel multifunctional SILCs gives an opportunity to develop sustainable fixed-bed reactors.

As far as this aforesaid issue is concerned, nanocatalysts may offer another approach to eliminate the gap between homogeneous and heterogeneous catalysts by preserving the desired attributes of both catalysts [13]. Among the heterogeneous nanocatalysts, palladium nanoparticles (PdNPs) have been a popular choice as nanocatalysts for sustainable organic transformations due to their amazing catalytic activity, selectivity, and physicochemical stability under different reaction conditions [14]. However, the primary limitation of employing the nascent PdNPs as catalysts is their aggregation, which significantly reduces their catalytic activity [14]. Therefore, various organic and inorganic materials have been widely applied as solid scaffolds to stabilize PdNPs and prevent their agglomeration as well [14]. To name a few, functionalized SBA-15 [15, 16, 17], modified biopolymers [18], organohydrogels [19], poly(ionic liquid) (PIL) [20], metal-organic frameworks (MOFs) [21, 22], iron-iron oxide [23], functionalized graphene oxide [24, 25], etc., have been used as effective solid supports for PdNPs in different catalytic reactions. However, paucity, preparation intricacy, toxicity, low stability, and low Pd-loading capacity, as well as palladium leaching, act as the major drawbacks of the majority of these solid supports, which limit their wider usage [14, 26]. As a result, there is a growing need to design and develop green solid supports that are sustainable, cost-effective, have tunable physical properties (porosity, crystallinity, and surface functionality), and have several active coordination sites for binding, good dispersibility, and stabilization of PdNPs in order to sustain their catalytic activity and address the aforementioned challenges.

Despite the amazing advantages of chitosan (CS) such as renewability, sustainability, the abundance of its resources, production cost-effectiveness, non-toxicity, and the availability of several chelating groups on its surface capable of stabilizing PdNPs, the poor mechanical stability of CS under catalytic conditions limits its wider-range catalysis application [27]. Several approaches to upgrading the mechanical properties of chitosan have been documented in the literature. Chemical cross-linking was at the forefront of these approaches, where the most common dialdehyde cross-linker "glutaraldehyde" was used to cross-link CS chemically [28, 29]. Further, grafting and blending of chitosan with some ionic liquids offer other strategies for enhancing chitosan's mechanical stability [30]. Moreover, the blending of nanomaterials with CS (particularly graphene family nanomaterials, such as graphene (GR), graphene oxide (GO), and reduced graphene oxide (RGO)) resulted in the formulation of nanocomposites of greatly elevated mechanical properties [31, 32]. Apart from enhancing the mechanical qualities of chitosan, GO has been shown to be an effective support material for a variety of metallic nanocatalysts, including Pd, Au, Fe<sub>3</sub>O<sub>4</sub>, and others [33, 34, 35]. It is primarily due to its unique structure, excellent coordination abilities, large surface area, high thermochemical stability, good metallic nanocatalyst loading capacity, and so on. Therefore, it will be interesting to prepare a novel nanocomposite compressing ionic liquid-grafted chitosan (ILCS) and magnetic graphene oxide (MGO) for the immobilization of PdNPs and the formation of a novel heterogeneous nanocatalyst with synergistically improved physicochemical and catalytic properties. To date, very few studies have been reported on the fabrication of ILCS/ MGO nanocomposites for application in the microextraction of endocrine-disrupting phenolic compounds [36],

biosorption of alkaloids [37], and as a scaffold for Pd nanoparticles in hydrogen generation from ammonia borane [38]. Nevertheless, there are no reports available on their application in reduction reactions.

Inspired by the aforementioned exceptional facts, I report herein for the first time the development of smart multifunctional nanocatalytic system based on carboxymethyl-imidazolium-grafted chitosan Schiff base (CMICSB), magnetic graphene oxide (MGO), and PdNPs. The catalytic performance of the novel heterogeneous nanocatalyst will be investigated in the nitroarenes reduction reactions. The motivation for selecting nitroarenes as targets for the new catalyst was their harmful impacts on public health and the environment. In addition, the importance of reduction products (aromatic amines) as intermediates in the synthesis of many important bioactive compounds, pharmaceuticals, agrochemicals, dyes, polymers, etc [39].

## 2. Materials And Methods

Specifications and suppliers of the chemical substances used in this study have been shown in the electronic supplementary materials (ESM). In addition, details of the techniques used in structural and morphological characterization of the synthesized compounds were also given in the ESM. Moreover, the experimental protocols applied for the preparation of GO, 1-(carboxymethyl)-3-(3-(4-formylphenoxy)propyl)-1H-imidazol-3-ium chloride ionic liquid (CMICIL), and carboxymethyl-imidazolium-grafted chitosan Schiff base (CMICSB), and were depicted in the ESM.

### 2.1. Synthesis of CMICSB-MGO nanocomposite (Support)

The ternary nanocomposite (**CMICSB-MGO**) was prepared by coupling GO with CMICSB through a protocol described previously by Anush et al. [40], with a slight modification. In brief, an aliquot of 1.0 g of CS was dissolved in a 2% aqueous acetic acid solution (100 mL) under vigorous stirring. CMFPIC ionic liquid (equivalent to the  $\text{NH}_2$ -content of CS calculated from N%) was gradually added to this solution while vigorously stirring, and the reaction mixture was kept at 60 °C while stirring for 6 h. Afterward, an aliquot of 0.5 g of GO was added to the reaction mixture and the content was ultrasonically pulsed for 6 h. The CMICSB-GO was precipitated by the addition of 200 mL of acetone to the reaction mixture. The CMICSB-GO was then filtered, washed 3 to 4 times with ethanol to remove the unreacted aldehyde, and later dried at 30 °C overnight. The CMICSB-MGO nanocomposite was prepared using a slightly modified hydrothermal approach. A solution of  $\text{FeCl}_2 \cdot 4\text{H}_2\text{O}$  (1.35 g) and  $\text{FeCl}_3 \cdot 6\text{H}_2\text{O}$  (2.03 g) in DIW (33 mL) was mixed with a dispersion of 1.35 g of CMICSB-GO in DIW (50 mL) under vigorous stirring. For 10 min, the solution was heated at 50 °C with continuous stirring. The pH of the reaction mixture was adjusted to 9 by adding 1 M NaOH at the same temperature and stirring. The reaction was kept at the same condition for a further 60 min. Finally, the reaction content was cooled down to room temperature, and the obtained brownish-black product (**CMICSB-MGO**) was magnetically collected, thoroughly washed with DIW, and dried overnight in a vacuum oven at room temperature. The successful formation of CMICSB-MGO was confirmed by spectral (FTIR, XRD, EDX), microscopic (SEM, TEM), and thermal (TGA) analyses.

## 2.2. *In situ* preparation of CMICSB-MGO-Pd nanocatalyst

The desired nanocatalyst was prepared following a method modified from the previously reported work [41]. Briefly, an aqueous dispersion (1 mg/mL) of the CMICSB-MGO support was prepared by ultrasonication and mixed with equal volume of ethanol followed by the addition of a certain amount of Pd(OAc)<sub>2</sub> to attain a reaction mixture ratio of support : Pd (4:1). This mixture was then stirred at 60 °C for 1 h. The obtained nanocomposites were magnetically or by centrifugation collected, thoroughly washed with DIW and then acetone, and dried overnight under vacuum at 60 °C. The successful formation of the nanocatalyst (**CMICSB-MGO-Pd**) was confirmed using spectral, microscopic, and thermal techniques.

## 2.3. Catalytic activity

### 2.3.1. *Performance in nitroarenes reduction*

The performance of the new nanocatalyst (CMICSB-MGO-Pd) in the catalytic reduction of nitroarenes was preliminarily investigated using a model reaction of the reduction of nitrobenzene (NB) by NaBH<sub>4</sub> in the presence of nanocatalyst. This reaction was performed under different conditions (catalyst dose and temperature) following a reduction protocol described in a previous study [25] to investigate the optimum catalytic conditions for new nanocatalyst. Briefly, aqueous solutions of NaBH<sub>4</sub> (1.0 – 2.0 mmol) and NB (1.0 mmol) were mixed in different solvents (5 mL). The obtained mixture was stirred for 1 min. Intermittent UV/Vis measurements were made to ensure that no reaction took place in the absence of a catalyst. Thereafter, an appropriate amount of **CMICSB-MGO-Pd** nanocatalyst (0 – 5 mg) was added under vigorous stirring at different temperatures (room temperature – 50 °C). To investigate the reduction reaction progress and the catalytic efficiency of the nanocatalyst, the reaction content was analyzed at definite time intervals by UV–Vis spectroscopy in the wavelength range of 200–360 nm. After completion of the catalytic reaction (monitored by TLC), the **CMICSB-MGO-Pd** nanocatalyst was magnetically or ultracentrifugally collected, thoroughly rinsed with DIW, and dried for reuse in the successive catalytic runs. The reduction product (aniline) was isolated by solvent evaporation under a reduced pressure. The optimum conditions determined by the model reaction were used to carry out the catalytic reduction of various nitroarenes. The column chromatography on silica gel eluting with a mixture of ethyl acetate/hexane (1:1) was used to further purify the crude aminoarene products.

### 2.3.2. *Heterogeneity of nanocatalyst*

The heterogeneity of the nanocatalyst was investigated using the hot filtration test. In brief, after performing the catalytic reaction, the nanocatalyst was discarded from the hot reaction mixture by filtration. The clear filtrate was then stirred for a further 1 h at 50 °C to observe the change in the productivity of aniline. It was observed that there was no remarkable change in the reaction or in the productivity of aniline in the absence of nanocatalyst, indicating the nanocatalyst heterogeneity.

## 2.4. *Statistical analysis*

SPSS 20.0 (SPSS Inc.) software was applied to perform the statistical analyses for the obtained data. These data were also subjected to one-way variance (ANOVA) and a multi-range test. Origin 9.1 (SR0 b215) has been used to represent the raw data into graphs. All results have been presented as mean  $\pm$  deviation, with a  $P$ -value of less than 0.05 being recognized as the significance limit.

## 3. Results And Discussion

### 3.1. Synthesis chemistry

Multiple chemical reactions have been used to prepare the key starting materials (GO, carboxymethyl imidazolium chloride ionic liquid (CMICIL), and CMICSB) required for the fabrication of the new nanocatalyst (CMICSB-MGO-Pd) (see **Scheme 1**). Initially, GO sheets were prepared through the oxidation of graphene (G) by a mixture of oxidizing agents. On the other hand, CMICIL was synthesized starting from 4-hydroxybenzaldehyde (4-HBA) *via* two successive reactions: (i) chloropropylation of 4-HBA to yield 4-(3-chloropropoxy)benzaldehyde (CPHBA) and (ii) quaternization of CPHBA with 1-imidazoleacetic acid to produce CMICIL. The Schiff base condensation of this ionic liquid with chitosan (CS) leads to the formation of the desired ionic liquid-grafted chitosan Schiff base (CMICSB). When this Schiff base condensation reaction was carried out in the presence of GO and under ultrasonic irradiation, the CMICSB-GO nanocomposite was formed due to a reaction between the OH group of CS and the COOH group of GO [40].

A modified thermal co-precipitation protocol was applied using the pre-prepared CMICSB-GO and ferric/ferrous chlorides to fabricate the magnetic nanocomposites support (CMICSB-MGO). For fabrication of the new heterogeneous nanocatalyst (CMICSB-MGO-Pd), the PdNPs were *in-situ* prepared by reduction of  $\text{PdCl}_4^{2-}$  with  $\text{NaBH}_4$  in the presence of CMICSB-MGO support. The PdNPs were simultaneously formed and immobilized in the support network.

## 3.2. Materials characterization

### 3.2.1. FTIR spectroscopy

**Fig. 1A** shows the FTIR spectra of the as-fabricated starting materials (GO, CMICSB), magnetic nanocomposite support (CMICSB-MGO), and new nanocatalyst (CMICSB-MGO-Pd). The characteristic GO absorption bands could be observed in its respective spectrum at 3311, 1715, 1604, 1425, 1236, and 1061  $\text{cm}^{-1}$  assignable to the stretching vibrations of O–H, C=O, C=C, carboxyl (C–O), epoxy (C–O–C) groups, respectively [42]. On the other hand, in the CMICSB spectrum, there can be seen peaks at 3233, 1705, 1613, 1029, and 832  $\text{cm}^{-1}$  which could be assigned to the stretching vibrations of OH/NH, carboxyl (C=O), azomethine/ amide (C=N/ C=O), glycosidic linkage (C–O–C), and imidazolium ring, respectively. Noteworthy, the peak intensity of 1715  $\text{cm}^{-1}$  for CMICSB-GO has remarkably decreased and a new peak has emerged at 1735  $\text{cm}^{-1}$ , which could be attributed to the ester linkage of the carboxyl group of GO with the OH group of CS chain [40]. As for the magnetic nanocomposite support, the almost

disappearance of the stretching vibration of GO carboxyl (C=O) group ( $1715\text{ cm}^{-1}$ ) coupled with emergence of two new peaks at  $1633\text{ (COO}^{-}\text{)}$  and  $578\text{ (Fe-O)}\text{ cm}^{-1}$  confirms the successful self-assembly of CMICSB-GO- $\text{Fe}_3\text{O}_4$  (CMICSB-MGO) [37]. Similarly, the FTIR spectrum of the CMICSB-MGO-Pd nanocatalyst showed a decrease in intensity and/or shift of the azomethine peak along with the emergence of two new peaks at  $595$  and  $442\text{ cm}^{-1}$  which are assigned as Pd-O and Pd-N groups, respectively. These findings imply the immobilization of PdNPs into the CMICSB-MGO network and the formation of the new nanocatalyst as shown in **Scheme 1**.

### 3.2.2. Raman spectroscopy

The Raman spectra of the new magnetic support (CMICSB-MGO) and nanocatalyst (CMICSB-MGO-Pd) are depicted in **Fig 1B**. Both nanocomposites display two characteristic peaks that are distinctive of the GO sheet [43]: the D-band, which is associated with disordered carbon or *K*-point phonons of  $A_{1g}$  symmetry; and the G-band, which is associated with the vibration of  $\text{sp}^2$ -bonded C-atoms in a 2D hexagonal lattice. For CMICSB-MGO, the D-band is observed at  $\sim 1346\text{ cm}^{-1}$ , while the G-band is centered at  $\sim 1585\text{ cm}^{-1}$ . As evident in the CMICSB-MGO-Pd spectrum, no significant change was observed in the position of D-band, whereas a red-shift (by  $+9\text{ cm}^{-1}$ ) was observed in the G-band after immobilization of the PdNPs. This shift could be ascribed to the alteration of local stress caused by the dispersion of PdNPs into the GO network [42]. Interestingly, the intensity ratio of the D to G band ( $I_D/I_G$ ) increased slightly from 0.95 in support to 1.01 in catalyst, implying that GO sheets dispersed well and PdNPs nucleated at their surfaces, resulting in defects in the GO structure [42, 44]. This relative change in  $I_D/I_G$  ratio is potential to improve the catalytic activity of nanocatalyst due to the more active sites by providing additional active sites via the flaws on the support surface.

### 3.2.3. PXRD analysis

The powder x-ray diffraction (PXRD) patterns of the as-prepared starting materials (GO, CS, CMICSB), and their nanocomposites (CMICSB-MGO and CMICSB-MGO-Pd) shown in **Fig S1–S2** (see **ESM**) and **Fig 1C**. The emergence of a characteristic diffraction peak at  $2\theta = 10.2^\circ$  in the GO spectrum (**Fig S1, ESM**) confirms the successful conversion of graphite into GO [45]. On the other hand, two diffraction peaks can be observed in the CS diffractogram at  $2\theta = 10.3^\circ$  and  $20.1^\circ$  (**Fig S2, ESM**) which could be relegated to the intramolecular and intermolecular H-bonding in the (020) and (200) reflection planes of chitosan [46]. In contrast, only one obvious peak appears in the CMICSB diffractogram at  $2\theta = 21.1^\circ$  (**Fig S2, ESM**), indicating a decrease in the H-bonding capability of CMICSB as a result of the grafting of CMICIL on its surface. As for the two magnetic nanocomposites (support and nanocatalyst) (**Fig 1C**), they exhibited multiple peaks centered at  $2\theta = 10.07^\circ$ ,  $30.11^\circ$ ,  $35.54^\circ$ ,  $43.41^\circ$ ,  $57.40^\circ$ , and  $62.27^\circ$  which are characteristic of GO as well as (220), (311), (400), (422), (511), and (440) lattice planes of  $\text{Fe}_3\text{O}_4$  nanoparticles [44]. Moreover, two peaks at  $2\theta = 40.1^\circ$  and  $68.2^\circ$  showed up for CMICSB-MGO-Pd which could be assigned to the (111) and (220) lattice planes of the face centered cubic (fcc) symmetry of PdNPs [47]. Other minor peak interferences may be caused by the existence of the ILCS in nanocomposites matrices.

### 3.2.4. Thermogravimetric analysis

The thermal stability of the new materials was investigated using thermogravimetric analysis (TGA) under an N<sub>2</sub> atmosphere, and the obtained results are represented in **Fig. 1D**. The TGA thermogram of GO exhibited three major thermal degradation stages. The first stage started at T > 45 °C with slight weight loss, which could be attributed to the vaporization of water molecules adhering to the GO sheets. In contrast, a significant weight loss has occurred in the second step (~150–400 °C) which might be related to the pyrolysis of labile oxygenated functional groups of GO (CO, C–O–C, and CO<sub>2</sub>), inducing disintegration of the GO network [42]. Above 400 °C, GO is finally burned out. Similarly, three successive weight loss steps with a final residue of ~17% can be seen in the thermogram of CMICSB at the temperature ranges of (46–154 °C), (155–395 °C), and (397–630 °C). These weight losses could be attributed to the liberation of H<sub>2</sub>O molecules, degradation of the CMICIL segment, and decomposition of CS chain, respectively. The CMICSB-GO displayed four weight-loss phases in its thermogram, leaving a final residual of about 45%. The initial two degradation phases, which started at about 42 °C and 130 °C, respectively, might be ascribed to the liberation of the physisorbed water or solvent molecules and the pyrolysis of oxygenated functional groups, respectively. The additional weight losses at 205 and 355 °C could be attributed to the decomposition of the IL side chain and the CS network, respectively [48]. Based on TGA findings, the CMICSB-GO exhibited remarkably higher thermal stability than its ingredients (CMICSB and GO). The TGA thermograms of the magnetic support (CMICSB-MGO) and nanocatalyst (CMICSB-MGO-Pd) showed three and four thermal events, leaving final residues of about 46% and 48%, respectively. Generally, these nanocomposites are more thermally stable than their precursors. Interestingly, the nanocatalyst is less thermally stable (steady up to 200 °C) than its support (steady up to 255 °C). This might be due to the catalytic degradative effect of the PdNPs on the magnetic support.

### 3.2.5. SEM, TEM and EDX

The morphology of the CMICSB-MGO hybrid and its magnetic nanocomposites (CMICSB-MGO and CMICSB-MGO-Pd) were inspected using scanning electron and transmission electron microscopy (SEM/TEM) techniques. As shown in **Fig. 2A**, CMICSB-GO exhibited a flake-like morphology in which the flakes are highly interconnected to form more packed aggregates as compared to native CMICSB (**Fig S3, ESM**). Noteworthy, no distinct layers of CMICSB or GO can be seen in the SEM and TEM images (**Fig. 2A, D**), indicating that CMICSB and GO are mutually interacted. The SEM image of CMICSB-MGO (**Fig. 2B**) displayed a lamellar and more aggregated morphology with no distinct observable Fe<sub>3</sub>O<sub>4</sub> nanoparticles. This aggregation could be attributed to the magnetic nature of Fe<sub>3</sub>O<sub>4</sub> NPs embedded in the CMICSB-MGO nanocomposites. As for the CMICSB-MGO-Pd nanocatalyst, a mixed flaky and lamellar morphology was observed for it, with PdNPs scattered as tiny bright dots on its surface (**Fig. 2C**). **Fig. 2D-F** shows the TEM images of the hybrid (CMICSB-GO) and its magnetic nanocomposites. The GO sheet can be seen in the TEM image of the CMICSB-GO hybrid (**Fig. 2D**) with darker spots that are indicative of the presence of ILCS. Similarly, the GO nanosheet can be detected in the TEM images of magnetic support and

nanocatalyst with  $\text{Fe}_3\text{O}_4$  (**Fig. 2E**) and  $\text{Fe}_3\text{O}_4/\text{PdNPs}$  (**Fig. 2F**) embedded into the nanosheets of support and nanocatalyst, respectively.

The energy-dispersive X-ray (EDX) technique was used to inspect the purity and chemical compositions of the new materials. The EDX spectrum of the CMICSB-GO hybrid (**Fig S4, ESM**) revealed the presence of C, O, N, and Cl elements in its microstructure. In addition to these peaks, elemental Fe peaks of  $\text{Fe}_3\text{O}_4$  NPs can be seen in the magnetic support spectrum, while elemental Fe of magnetite and Pd ( $L\alpha$ )/ Pd ( $L\beta$ ) peaks of PdNPs can be seen in their EDX spectra (**Fig. 3A,B**). The Pd content in the new nanocatalyst was estimated using the inductively coupled plasma atomic emission spectroscopy (ICP-AES) and was found to be 21.59 wt%. This extremely high Pd loading capacity could be attributed to the presence of multiple chelating active sites on the magnetic support surface capable of tightly binding PdNPs and preventing their leaching, such as hydroxyl, carboxyl, azomethine, and imidazolium moieties.

## 3.3. Catalytic study

### 3.3.1. Catalytic reduction of nitrobenzene

The catalytic reduction of nitrobenzene ( $\text{PhNO}_2$ , NB) into aminobenzene ( $\text{PhNH}_2$ , AB) was chosen as a model reaction to study the catalytic performance of the CMICSB-MGO-Pd nanocatalyst in reduction processes. Notably, NB is a crucial material in several industries like drugs, oils, dyes, and pesticides, as well as being a by-product of numerous industrial processes [49]. As a result, industrial effluents always contain very high concentrations of NB that exert many harmful impacts on aquatic life [48]. Therefore, conversion of the toxic NB into another valuable product like AB is of great importance. To that end, the catalytic activity of the new nanocatalyst in the reduction of toxic NB into AB was studied in the presence of  $\text{NaBH}_4$  under different conditions to find the optimum parameters for catalyst performance. Based on the findings in Table S1 (ESM), the following parameters were defined as the optimum conditions for catalytic performance: 1.5 mmol  $\text{NaBH}_4$ ; 3.0 mg catalyst; room temperature (RT). Under optimum conditions, UV-Vis measurements were used to monitor the NB reduction reaction in order to determine the ideal period for maximum aminoarene production. As shown in **Fig. 4A**, the standard NB sample exhibited an intense UV-Vis absorption peak at  $\lambda_{\text{max}} = 268$  nm, whereas, the standard AB sample showed two characteristic absorption peaks at  $\lambda_{\text{max}} = 231$  and 280 nm [50]. **Fig. 4B** shows the time-dependent UV-Vis spectra of reduction of NB in the presence of CMICSB-MGO-Pd nanocatalyst and  $\text{NaBH}_4$ . Upon reaction progress with time, it occurs that significant declines in the intensity of the peak distinctive of NB at  $\lambda_{\text{max}} 268$  coupled with a simultaneous increase in the intensity of the absorption peak at 231 nm ( $\lambda_{\text{max}}$  of AB) with an isosbestic point at 244 nm, due to catalytic conversion of NB into AB. Noteworthy, as AB absorbs at 280 nm, the  $\lambda_{\text{max}}$  of NB remarkably decreases and slightly red-shifts once catalysis progresses and AB is formed. The NB was almost completely converted (~99%) to AB within 7.5 min under optimum conditions. The reduction of NB was also performed in the absence of nanocatalyst as a control experiment, and the UV-vis spectrum showed no decrease in characteristic peak intensity ( $\text{NO}_2$ ) at 268 nm with time (**Fig. 4C**). In contrast, the intensity of this peak was dramatically decreased till reaching

a steady phase within 7.5 min (NB is completely reduced to AB) when the NB reduction was performed in the presence of a nanocatalyst. These results suggest the effective and amazing role of CMICSB-MGO-Pd in the reduction of the NB/ $\text{NaBH}_4$  substrate.

The findings of the kinetic study for the catalytic reduction of NB over CMICSB-MGO-Pd nanocatalyst demonstrated that these data are fitted well with the pseudo-first-order kinetic model as revealed by the linear correlation with  $R^2 = 0.99604$  of  $\ln(C_t/C_0)$  *verse* reaction time with an apparent rate constant  $k = 0.43962 \text{ min}^{-1}$  (Fig. 4D).

### 3.3.2. Catalytic reduction of nitrobenzene derivatives (nitroarenes)

To validate the generality and limitations of the new nanocatalyst in nitroarenes reduction reactions, several catalytic reactions were performed using different substrates to study the effect of the substrate structure on the nanocatalyst performance and the aminoarenes productivity. As shown in **Table 1**, the rate of reduction reaction and its productivity are remarkably affected by changes in the electronic and steric properties of nitroarene. Generally, the products of catalytic reactions (aminoarenes) were obtained in high to excellent yields (from 93 to > 99) within 3–15 minutes. The catalytic performance is remarkably affected by the nature and position of the substituent on the nitrobenzene derivatives. For instance, as previously documented in the literature [51, 52], the good exchange dynamics between substrate and the product within the catalyst network during the course of the catalytic reaction leads to higher catalytic conversion and, consequently, greater yield. The dynamics of this exchange depends on the fit between the molecular structure of the substrate/ product and the cavities in the catalyst network, which is strongly correlated to the steric hindrance exerted by the phenyl substituents. For examples, the bad fit of the nitroarenes and aminoarenes with bulky groups (I **Entry 4**, Br **Entry 3**) with CMICSB-MGO-Pd cavities is probably responsible for their higher catalytic conversion as compared to chloro derivatives (**Entry 2**, **Table 1**). Meanwhile, the bad compatibility between the bent structures of *ortho*- and *meta*-isomers with CMICSB-MGO-Pd cavities as compared to the liner structures of *para*-isomers is probably responsible for the promoted exchange dynamics and consequently higher catalytic conversion (**Entries 4-8**, **Table 1**) [51,52]. On the other hand, the reduction of 2-nitroacetophenone, 2-nitrobenzaldehyde, and 2-nitrobenzoic acid chemoselectivity of the new nanocatalyst for reduction of  $\text{NO}_2$  functional group in the presence of other reducible substituents (**Entries 9-11**, **Table 1**). The findings proved that the developed nanocatalyst exhibited high chemoselective reduction toward the  $\text{NO}_2$  group. However, all attempts to execute chemoselective reduction of one  $\text{NO}_2$  group in the presence of another failed, and a mixture of reduction products was obtained (**Entry 13**, **Table 1**). The reduction of aliphatic nitro compound (nitrocyclohexane) was almost completed within 5 minutes (**Entry 16**, **Table 1**).

In addition, the catalytic activity level of new nanocatalyst was further investigated based on the values of turnover frequency (TOF) (moles of nitroarene converted by the unit nanocatalyst per unit time). The TOF values of CMICSB-MGO-Pd were in the range of  $1257 - 2089 \text{ min}^{-1}$  (see **Table 1**). These extremely high TOF values could be attributed to the increase in PdNPs loading (21.59 wt%), which could be

entrapped by many active binding sites on the surface of CMICSB and GO (carboxyl, amino, hydroxyl, azomethine). Hence, the PdNPs are highly distributed on the surface of the magnetic support, which allows them to be in direct contact with the reaction substrate (nitroarenes) (see **Fig. 5**). As a result, the utilization ratio of Pd increases and, accordingly, the TOF value increases.

### 3.3.3. Proposed reduction mechanism

According to the previous studies [<sup>53,54,55</sup>], a possible chemical pathway for the reduction of nitroarenes using NaBH<sub>4</sub> mediated by the CMICSB-MGO-Pd nanocatalyst is depicted in **Fig. 5**. Several intermediates are formed during the course of the reduction reaction. In the beginning, the borohydride (BH<sub>4</sub><sup>-</sup>) ions are adsorbed on the PdNPs surface, which subsequently undergoes hydrolytic cleavage mediated by PdNPs to form active hydrogen molecules adhered to the PdNPs. Concurrently, the nitroarene substrate is adsorbed onto the nanocatalyst surface and reduced *via* hydride transfer to generate an active nitroso derivative. This active intermediate is subjected to two consecutive hydrogen transfer processes to produce the targeted aminoarene *via* a hydroxylamine intermediate.

Table 1

The catalytic performance of the CMICSB-MGO-Pd nanocatalyst in nitroarenes reduction reactions under the optimum conditions <sup>a</sup>

Entry <sup>a</sup>	Substrate	Product	Time (min) <sup>b</sup>	Yield%	TOF (min <sup>-1</sup> )
1	Nitrobenzene	Aniline	7.5	99	1709
2	1-Chloro-2 nitrobenzene	2-Chloroaniline	9	97	1699
3	1-Bromo-2 nitrobenzene	2- Bromoaniline	7.0	99	1830
4	1-Iodo-2 nitrobenzene	2-Iodoaniline	3.0	> 99	2089
5	1-Iodo-4 nitrobenzene	4-Iodoaniline	10	94	1785
6	2-Nitrophenol	2-Aminophenol	7.0	> 99	1856
7	3-Nitrophenol	3-Aminophenol	7.0	99	1744
8	4-Nitrophenol	4-Aminophenol	7.5	97	1648
9	2-Nitroacetophenone	2-aminoacetophenone	9.0	96	1480
10	2-Nitrobenzoic acid	2-aminobenzoic acid	9.0	95	1394
11	2-Nitrobenzaldehyde	2-aminobenzaldehyde	12.0	93	1257
12	2-nitroaniline	o-phenyldiamine	6.5	> 99	1861
13	o-dinitrobenzene	o-phenyldiamine	8	> 99	1775
14	2-Nitrotoluene	2-Aminotoluene	9	94	1425
15	1-Nitronaphthalen	1-Aminonaphthalen	6	98	1800
16	Nitrocyclohexane	Aminocyclohexane	5	99	1876
<sup>a</sup> General conditions: Nitroarene (1.0 mmol); Nanocatalyst (3 mg); NaBH <sub>4</sub> (1.5 mmol); DIW/EtOH (1:1) (2 mL); Room temperature (RT).					
<sup>b</sup> Reaction time was determined using TLC.					

### 3.3.4. Nanocatalyst recoverability and reusability

From an economic and environmental point of view, recoverability and reusability are very important merits of heterogeneous catalysts, where catalysts with high recoverability and reusability are particularly desirable for large-scale synthesis applications. Further, Pd leaching from the nanocatalyst surface after few runs may result in several problems, such as reduced catalytic activity, obtaining impure products, and environmental pollution with Pd impurities. Therefore, the reusability of CMICSB-MGO-Pd and potential Pd leaching was investigated in the catalytic reduction of nitrobenzene. The NB was almost completely converted into AB (99% conversion) within 7.5 min using a fresh nanocatalyst in the 1st catalytic reduction cycle. This nanocatalyst can be recycled up to eight successive cycles without a

significant loss in NB to AB conversion (from 99 to ~ 93%, i.e., a 7% catalytic activity drop) (Fig. 6). However, after eight catalytic runs, the catalytic performance declined to ~ 83%, but the physicochemical stability of the catalyst still held up well. The ICP-AES experiment reveals that only a very little amount of Pd was leached from the solid CMICSB-MGO support (0.29%).

### 3.3.5. What is the new nanocatalyst's rank in comparison to previously reported ones?

To gain more information about the feasibility of new nanocatalyst for large-scale catalytic applications, a comparison of the findings of this work with the previously reported studies has been performed (see Table 1). By comparing our nanocatalyst's catalytic activity to that of the top previously reported catalytic systems in the literature, we find it to be exceptional in the reduction of 4-nitrophenol (4-NP) into 4-aminophenol (4-AP). According to the TON and  $k_{obs}$  values for the CMICSB-MGO-Pd nanocatalyst, the activity of the new nanocatalyst was superior to the majority of previously reported Pd NP-encapsulated catalysts. The amazing catalytic performance of CMICSB-MGO-Pd was due to the superior structural characteristics of CMICSB-MGO, as well as the high usage of PdNPs.

Table 2

Comparison of the catalytic performance indices for the reduction of 4-NP over PdNPs-based catalysts over different supports

Catalyst	Conditions				Yield (%)	$k_{app}$ ( $\text{min}^{-1}$ )	TOF ( $\text{min}^{-1}$ )	Ref.
	Cat. (mg)	$\text{NaBH}_4$ (mg)	Temp.	Time (min)				
Pd/GNS-NH <sub>2</sub>	5	100	55	180	91.5	–	65.90	[56]
CPG	5	151	RT	300	99	–	1.19	[57]
CS/rGO/Pd	125	50	RT	3.0	> 99	–	0.33	[43]
Pd/Fe <sub>3</sub> O <sub>4</sub> /CS/GO	555	329	RT	20	86	0.414	311.0	[48]
Pd/CNT/CS/GO	124	328	RT	16	98	0.627	603.6	[48]
Pd/Fe <sub>3</sub> O <sub>4</sub> /CNT/CS/GO	5	328	RT	20	95	0.414	1590.0	[48]
Pd/CNT/CS hydrogel	555.5	41.5	RT	35	95	0.218	0.035	[58]
Fe <sub>3</sub> O <sub>4</sub> /CS-Me@Pd	10	75	RT	30	91	–	–	[59]
Fe <sub>3</sub> O <sub>4</sub> @Tr-CS@NNN-Pd	70	151	RT	7	98	0.0064	840	[60]
CMICSB-MGO-Pd	3	56	RT	7.5	98	0.440	1648	Our work

## Conclusion

This study succeeded in fusing different chemical approaches to design and fabricate new magnetic nanocomposite (CMICSB-MGO) comprising carboxymethyl-imidazolium-grafted chitosan Schiff base (CMICSB), graphene oxide (GO), and magnetite ( $\text{Fe}_3\text{O}_4$ ). The multiple active binding sites (carboxyl, amino, hydroxyl, azomethine) on the surface of this nanocomposite make it an efficient heterogeneous support for PdNPs to fabricate other a new magnetic nanocomposite (CMICS-MGO-Pd). The new magnetic nanocomposites (CMICSB-MGO and CMICS-MGO-Pd) were characterized based on spectral, thermal, and microscopic methods. The activity of the CMICS-MGO-Pd nanocatalyst was investigated in the catalytic reduction of hazardous nitroarenes by  $\text{NaBH}_4$  into useful aminoarenes. The magnetic nanocatalyst shows excellent catalytic activity, superior recoverability, as well as outstanding reusability in nitroarenes reduction reactions. In addition, this nanocatalyst demonstrated several additional merits, such as eco-friendship, good thermal stability, low leaching of PdNPs into the environment, use of a green solvent (water), short reaction times, excellent yields, amazing recyclability (up to 8 catalytic runs), and manufacturing cost-effectiveness. Consequently, the new green low-cost ionic nanocomposite may offer up new opportunities for chemical transformations with the new ionic nanocatalyst. Moreover, the CMICSB-MGO nanocomposite will also be a good bio-reductant platform for the creation and stabilization of metal nanoparticles, as well as highly effective and low-cost earth-abundant nanocatalysts for organic transformation processes.

## References

- 1 J. Becker, C. Manske, S. Randl, *Curr. Opin. Green Sustain. chem.* 100562 (2021).
- 2 M. Nasrollahzadeh, M. Sajjadi, S. Irvani, R.S. Varma, *J Hazard. mater* 401, 123401 (2021).
- 3 M. Ghobadi, M. Kargar Razi, R. Javahershenas, M. Kazemi, *Synth. Commun.* 51, 647-669 (2021).
- 4 M. Pagliaro, V. Pandarus, R. Ciriminna, F. Béland, P.D. Carà, *ChemCatChem*, 4, 432-445 (2012).
- 5 B. Panchal, Z. Zhu, S. Qin, T. Chang, Q. Zhao, Y. Sun, C. Zhao, J. Wang, K. Bian, S. Rankhamb, *Renew. Energy* 181, 341-354 (2022).
- 6 Z.J. Li, J.F. Sun, Q.Q. Xu, J.Z. Yin, *ChemCatChem*, 13, 1848-1866 (2021).
- 7 S. Sadjadi, *J. Mol. Liq.* 323, 114994 (2021).
- 8 A. Wolny, A. Chrobok, *Nanomaterials* 11, 2030 (2021).
- 9 E.N. Kusumawati, T. Sasaki, *Chem. Record* 19, 2058-2068 (2019).
- 10 J. Li, Z. Yang, S. Li, Q. Jin, J. Zhao, *J. Ind. Eng. Chem.* 82, 1-16 (2020).
- 11 M. Nasrollahzadeh, M. Ghasemzadeh, H. Gharoubi, Z. Nezafat, *J. Mol. Liq.* 342, 117559 (2021).

- 12 S. Kargar, D. Elhamifar, A. Zarnegaryan, *Surf. Interfaces* 23, 100946 (2021).
- 13 S.H. Gebre, *Appl. Nanosci.* 1-49 (2021).
- 14 M. Aksoy, H. Kilic, B. Nişancı, Ö. Metin, *Inorg. Chem. Front.* 8, 499-545 (2021).
- 15 S. Rostamnia, K. Lamei, F. Pourhassan, *RSC Adv.* 4, 59626-59631 (2014).
- 16 H. Alamgholiloo, S. Rostamnia, N. N. Pesyan, *Appl. Organomet. Chem.* 34, e5452 (2020).
- 17 S. Rostamnia, E. Doustkhah, B. Zeynizadeh, *Microporous Mesoporous Mater.* 222, 87-93 (2016).
- 18 A. Wolfson, E. Stamker, O. Levy-Ontman, *J. Appl. Polym. Sci.* 139, 51517 (2022).
- 19 M. Zhang, T. Zhao, C. Yu, Q. Liu, G. Wang, H. Yang, M. Yang, L. Jiang, M. Liu, *Nano Res.* 1-7 (2021).
- 20 Z. Zhang, H. Gai, Q. Li, B. Feng, M. Xiao, T. Huang, H. Song, *Chem. Eng. J.* 429, 132224 (2022).
- 21 S. Sadjadi, F. Koohestani, *J. Mol. Struct.* 1250, 131793 (2022).
- 22 S. Rostamnia, H. Alamgholiloo, X. Liu, *J. Colloid Interf. Sci.* 469, 310-317 (2016).
- 23 W.-J. Wang, F. Roberts, S. Peterson, S. Ha, L. Scudiero, R. Coustel, M. Mallet, M. Abdelmoula, C. Ruby, *Chem. Eng. J.* 427, 131763 (2022).
- 24 M. Mirza-Aghayan, M. Mohammadi, R. Boukherroub, *J. Organomet. Chem.* 957, 122160 (2022).
- 25 H. Alamgholiloo, S. Rostamnia, N.N. Pesyan, *Colloids Surf. A Physicochem. Eng.* 602, 125130 (2020).
- 26 M. Zhao, Y. Wu, J.P. Cao, *Appl. Organomet. Chem.* 34, e5539 (2020).
- 27 A. El Kadib, *ChemSusChem*, 8, 217-244 (2015).
- 28 M.I. Wahba, *J. Biomater. Scie. Polym. Ed.* 31, 350-375 (2020).
- 29 J.L. Sanchez-Salvador, A. Balea, M.C. Monte, C. Negro, A. Blanco, *Int. J. Biol. Macromol.* 178, 325-343 (2021).
- 30 A.A. Shamsuri, K. Abdan, T. Kaneko, *Molecules*, 26, 216 (2021).
- 31 D.C. Alves, B. Healy, T. Yu, C.B. Breslin, *Materials*, 14, 3655 (2021).
- 32 R. Ikram, B. Mohamed Jan, M. Abdul Qadir, A. Sidek, M.M. Stylianakis, G. Kenanakis, *Polymers*, 13, 3266 (2021).
- 33 Y. Yan, W.I. Shin, H. Chen, S.-M. Lee, S. Manickam, S. Hanson, H. Zhao, E. Lester, T. Wu, C.H. Pang, *Carbon Lett.* 1-23 (2020).

- 34 J. Soni, A. Sethiya, N. Sahiba, S. Agarwal, *Appl. Organomet. Chem.* 35, e6162(2021).
- 35 N. Yilmaz Baran, T. Baran, M. Çalışkan, *Ceramics Int.* 47, 27736-27747 (2021).
- 36 J. Shah, M.R. Jan, *J. Polym. Environ.* 28, 1673-1683 (2020).
- 37 T. Tang, S. Cao, C. Xi, Z. Chen, *Carbohydr. Polym.* 255, 117338 (2021).
- 38 H. Jia, Y. Zhu, X. Song, X. Zheng, P. Liu, *Int. J. Hydrog. Energy* 43, 19939-19946 (2018).
- 39 H.K. Kadam, S.G. Tilve, *RSC Adv.* 5(101), 83391-83407 (2015).
- 40 S.M. Anush, H.R. Chandan, B.H. Gayathri, Asma, N. Manju, B. Vishalakshi, B. Kalluraya, *Int. J. Biol. Macromol.* 164, 4391-4402 (2020).
- 41 L.K. Parrott, E. Erasmus, Fuller. *Nanotub. Carbon Nanostructures* 29, 527-539 (2021).
- 42 J. Song, X. Wang, C.-T. Chang, *J. Nanomaterials* 2014 (2014).
- 43 R. Bhaskar, H. Joshi, A.K. Sharma, A.K. Singh, *ACS Appl. Mater. Interfaces*, 9, 2223-2231 (2017).
- 44 S. Dhanavel, T. Revathy, A. Padmanaban, V. Narayanan, A. Stephen, *J. Mater. Sci.: Mater. Electronics*, 29, 14093-14104 (2018).
- 45 M.S. Samuel, S.S. Shah, V. Subramaniyan, T. Qureshi, J. Bhattacharya, N.P. Singh, *Int. J. Biol. Macromol.* 119, 540-547 (2018).
- 46 G.L. Clark, A.F. Smith, *J. Phys. Chem.* 40(7), 863-879 (1936).
- 47 R. Yahya, R.F.M. Elshaarawy, *React. Funct. Polym.* 170, 105137 (2022).
- 48 S. Sadjadi, M. Raja, *Int. J. Biol. Macromol.* 122, 228-237 (2019).
- 49 T. Li, X. Deng, J. Wang, Y. Chen, L. He, Y. Sun, C. Song, Z. Zhou, *Mar. Pollut. Bull.* 89, 384-389 (2014).
- 50 J. Liu, R. Ye, J. Shi, H. Wang, L. Wang, P. Jian, D. Wang, *Chem. Eng. J.* 419, 129640 (2021).
- 51 K. Harata, *Chem. Rev.* 98(5), 1803-1828 (1998).
- 52 S. Menuel, B. Léger, A. Addad, E. Monflier, F. Hapiot, *Green Chem.* 18(20), (2016) 5500-5509.
- 53 S. El-Hout, S. El-Sheikh, H.M. Hassan, F.A. Harraz, I. Ibrahim, E. El-Sharkawy, *Appl. Catal. A: General* 503, 176-185 (2015).
- 54 M. Li, G. Chen, *Nanoscale* 5(23), 11919-11927 (2013).

55 H. Veisi, B. Karmakar, T. Tamoradi, R. Tayebee, S. Sajjadifar, S. Lotfi, B. Maleki, S. Hemmati, *Sci. Rep.* 11(1), 4515 (2021).

56 H.G. Soğukömeroğulları, Y. Karataş, M. Celebi, M. Gülcan, M. Sönmez, M. Zahmakiran, *J. Hazard. Mater.* 369, 96-107 (2019).

57 H.G. Bilgicli, H. Burhan, F. Diler, K. Cellat, E. Kuyuldar, M. Zengin, F. Sen, *Micropor. Mesopor. Mater.* 296, 110014 (2020).

58 J. Zhu, X. Zhang, Z. Qin, L. Zhang, Y. Ye, M. Cao, L. Gao, T. Jiao, *Colloids Surf. A: Physicochem. Eng. Asp.* 611, 125889 (2021).

59 G. Wang, K. Lv, T. Chen, Z. Chen, J. Hu, *Int. J. Biol. Macromol.* 184, 358-368 (2021).

60 F. Rafiee, M. Rezaee, *React. Funct. Polym.* 172, 105208 (2022).

## Scheme

Schemes 1 is available in the Supplementary Files section.

## Figures

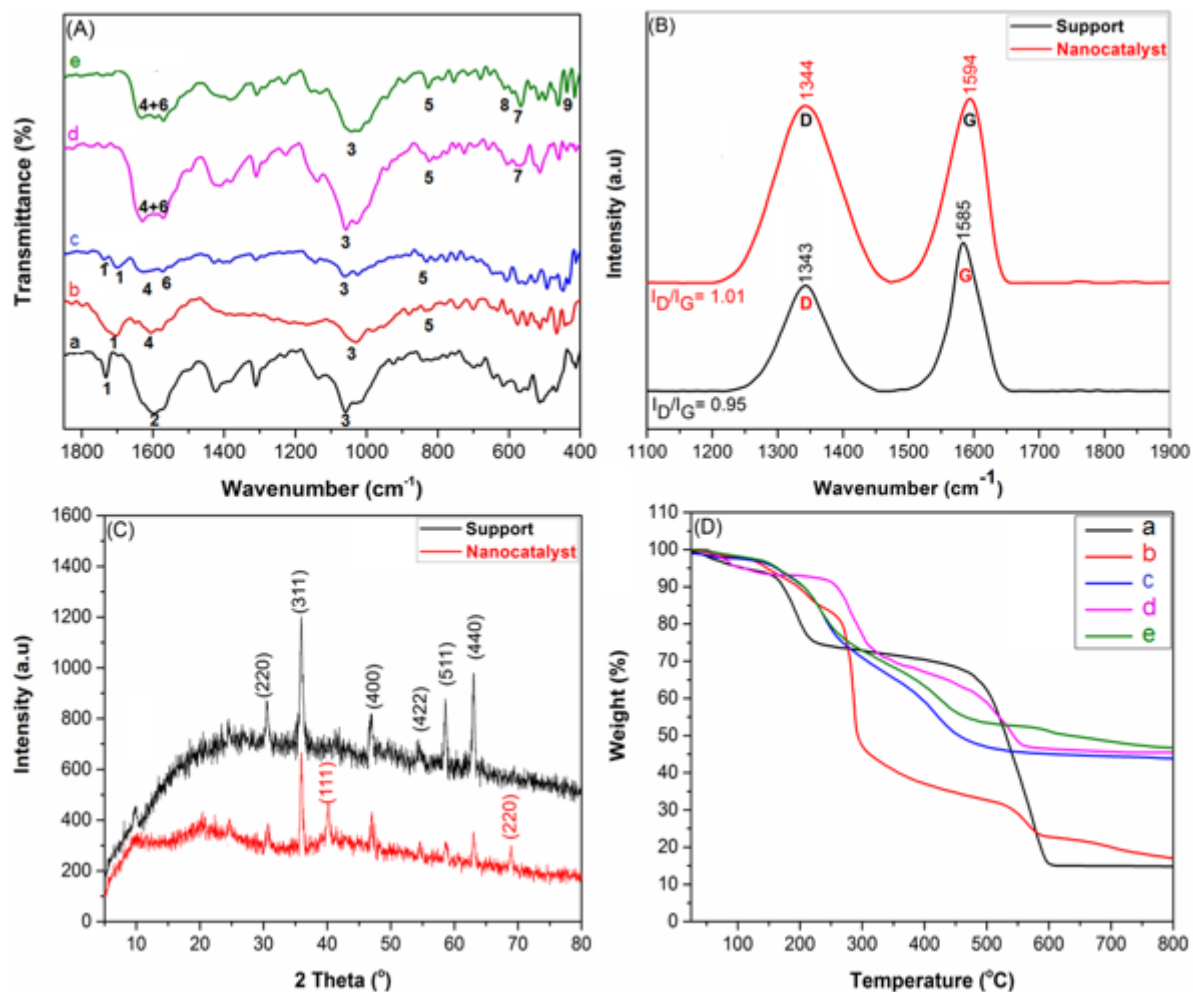


**Figure 1**

(A) FTIR spectral regions of the as-fabricated starting materials (GO, CMICSB, CMICSB-GO), magnetic nanocomposite support (CMICSB-MGO), and new nanocatalyst (CMICSB-MGO-Pd). Characteristic vibration peaks: (1) C=O ester; (1) C=O; (2) C=C; (3) epoxy (C–O–C); (4) amide I and azomethine (–CH=N–); (5) imidazolium ring; (6) CONH; (7) Fe–O; (8) Pd–O; (9), Pd–N. (B) Raman spectra of the magnetic support (ILCS@MGO) and the resultant nanocatalyst (ILCS@MGO@Pd). (C) PXRD spectra of the ILCS@MGO and ILCS@MGO@Pd nanocatalyst. (D) TGA thermographs of the starting materials (GO, CMICSB, CMICSB-GO), magnetic support (CMICSB-MGO), and nanocatalyst (CMICSB-MGO-Pd). Hint: a- GO, b- CMICSB, c- CMICSB-GO, d- CMICSB-MGO, and e- CMICSB-MGO-Pd.

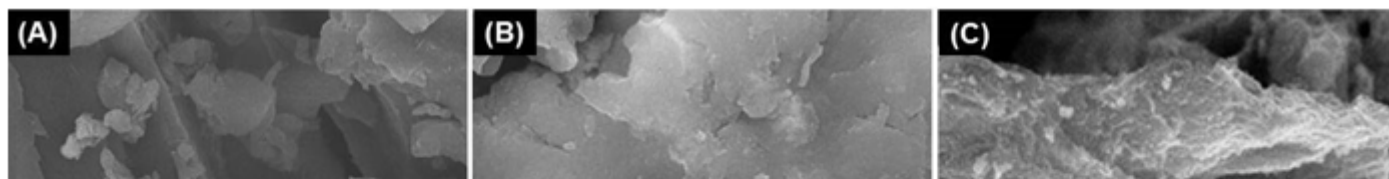


**Figure 2**

(A – C) SEM micrographs of the CMICSB-GO hybrid, CMICSB-MGO support, and CMICSB-MGO-Pd nanocatalyst, respectively. (D – F) TEM images of the hybrid, support, and nanocatalyst, respectively.

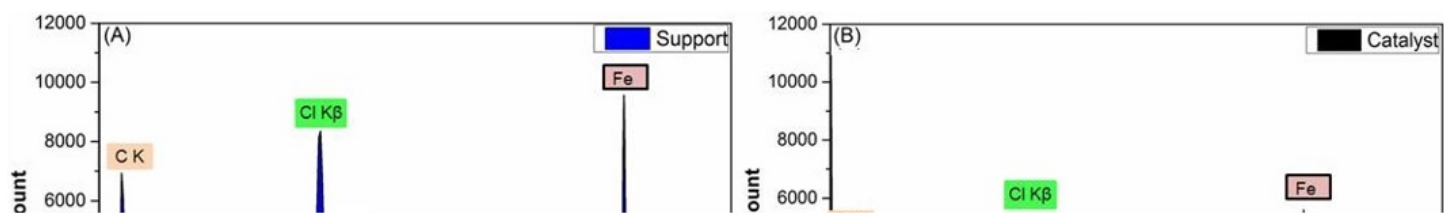


**Figure 3**

EDX spectra of (A) CMICSB-MGO support and (C) CMICSB-MGO-Pd nanocatalyst.

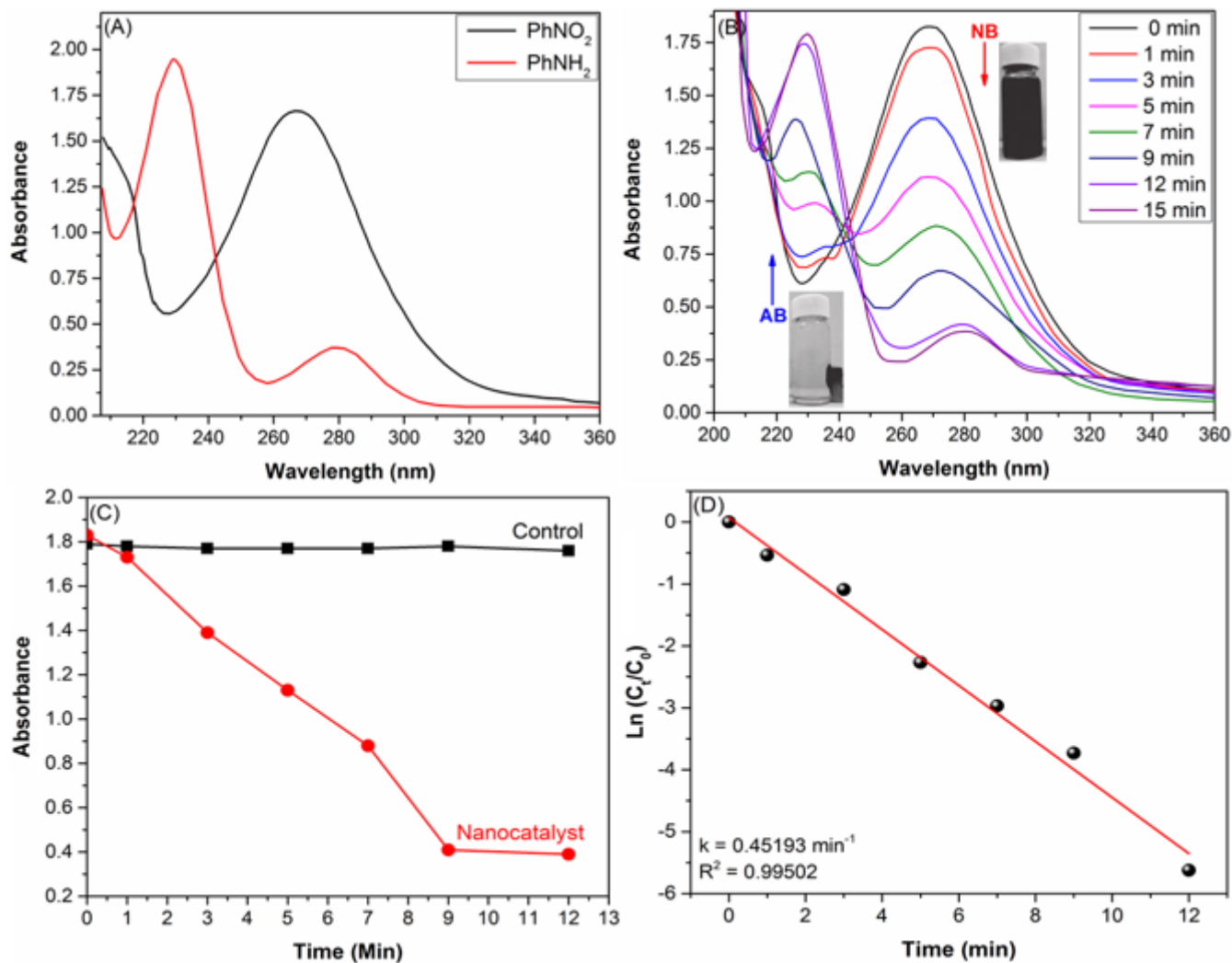


Figure 4

(A) UV-Vis spectra for the standard NB and AB samples. (B) UV-Vis spectra for the time-dependent reduction of NB into AB by  $\text{NaBH}_4$  in the presence of CMICSB-MGO-Pd nanocatalyst. (A) Kinetic study on the progress of reduction NB. The reaction conditions are: NB = 0.3 mmol, nanocatalyst = 1 mol%, and  $T = 40^\circ\text{C}$ .

Figure 5

Proposed mechanism for the reduction of nitrobenzene by  $\text{NaBH}_4$  over CMICSB-MGO-Pd nanocatalyst.

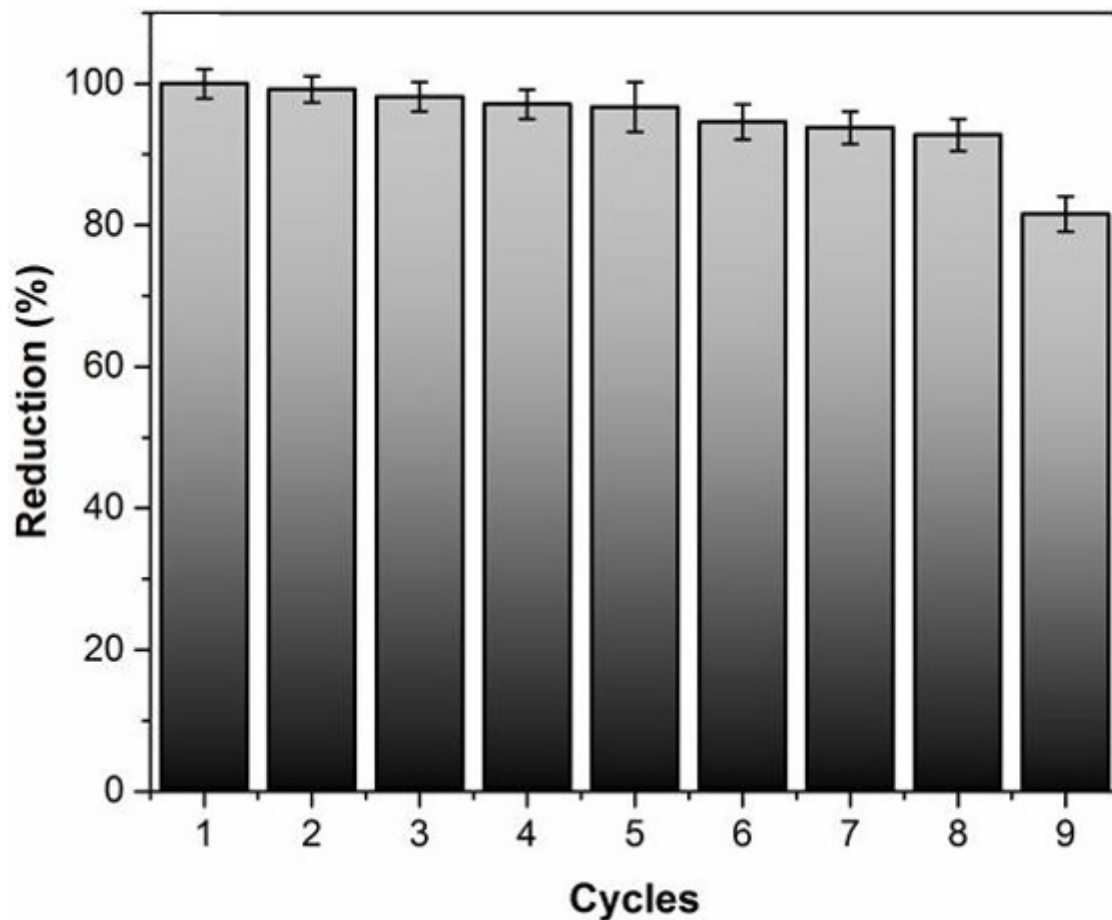


Figure 6

Reusability of new nanocatalyst (CMICSB-MGO-Pd) under optimal reaction conditions for NB reduction into AB. The NB to AB conversion and reduction% was estimated using UV-Vis spectroscopy.

## Supplementary Files

This is a list of supplementary files associated with this preprint. Click to download.

- [Scheme1.png](#)
- [CMICSBMGOPdJIOMPM22ESM.pdf](#)